IEICE TRANS. COMMUN., VOL.E107–B, NO.11 NOVEMBER 2024

PAPER

DDMA-MIMO/Capon Observations Using the MU Radar: Beamwidth Verification Using the Moon's Reflection

Tomoya MATSUDA[†a)], ***Nonmember***, **Koji NISHIMURA**[††], ***and*** **Hiroyuki HASHIGUCHI**[††], ***Members***

SUMMARY Phased-array technology is primarily employed in atmospheric and wind profiling radars for meteorological remote sensing. As a novel avenue of advancement in phased-array technology, the Multiple-Input Multiple-Output (MIMO) technique, originally developed for communication systems, has been applied to radar systems. A MIMO radar system can be used to create a virtual receive antenna aperture plane with transmission freedom. The MIMO technique requires orthogonal waveforms on each transmitter to identify the transmit signals using multiple receivers; various methods have been developed to realize the orthogonality. In this study, we focus on the Doppler Division Multiple Access (DDMA) MIMO technique by using slightly different frequencies for the transmit waveforms, which can be separated by different receivers in the Doppler frequency domain. The Middle and Upper atmosphere (MU) radar is a VHF-band phased array atmospheric radar with multi-channel receivers. Additional configurations are necessary, requiring the inclusion of multi-channel transmitters to enable its operation as a MIMO radar. In this study, a comparison between the brightness distribution of the beamformer, utilizing echoes reflected from the moon, and the antenna pattern obtained through calculations revealed a high degree of consistency, which means that the MU radar functions effectively as a MIMO radar. Furthermore, it is demonstrated that the simultaneous application of MIMO and Capon techniques has a mutually enhancing effect.

key words: *atmospheric radar, Capon beamformer, Doppler Division Multiple Access, phased array, MIMO*

1. Introduction

The phased-array radar technology, originally developed as a defense radar, has been primarily utilized for atmospheric and wind profiling radars. It has also been employed as a weather radar for research purposes. As a further development of the phased-array technology, the Multiple-Input Multiple-Output (MIMO) technique, which was originally developed for communication systems, has been applied to radars, making a new contribution for radar signal processing [1].

More recently, various phased-array applications that perform Digital Beam Forming (DBF) with multiple receivers have been developed. DBF provides multiple receive beams in a single scan, which dramatically reduces the scan time. However, conventional phased array radars cannot distinguish transmit signals at the receivers. Therefore, they are categorized as Single-Input Multiple-Output (SIMO) radars.

Manuscript received November 18, 2023.
Manuscript revised March 9, 2024.
Manuscript publicized May 6, 2024.

[†]Mitsubishi Electric Corporation, Amagasaki-shi, 661-8661 Japan.
[††]Kyoto University, Uji-shi, 611-0011 Japan.
a) E-mail: matsuda.tomoya.b30@kyoto-u.jp

DOI: 10.23919/transcom.2023EBP3182

The MU radar [2], [3], which has been operational for four decades years, is one of the most advanced atmospheric radars with 475 transmitters, phase shifters, and corresponding antennas to orient the beam direction electrically. The MU radar has mostly been operated as a SIMO radar, although it can also be operated as a MIMO radar with additional settings.

The orthogonality of the transmit signals is the most definitive difference between SIMO and MIMO radars. Phased-array radars that separate transmit waves can be referred to as multiple-input transmitters, and understanding the methodology of separating transmit waves from the receive signals. The transmit waves can be separated by adopting orthogonal waveforms for each transmitter. Some methods to achieve their orthogonality were introduced in [4]. It is necessary to select an appropriate method according to the application and transmit frequency characteristics.

A MIMO approach for atmospheric radars was applied in [5], [6] for atmospheric and ionospheric synthesis radar imaging observation, attempting to use Time Division Multiple Access (TDMA), Code Division Multiple Access (CDMA), and polarization diversity. We used the Doppler Division Multiple Access (DDMA) method, which utilizes a slow-time direction to obtain the orthogonal transmit waveforms [4], [7], [8].

The effectiveness of DDMA-MIMO radar was introduced in [9], demonstrating the beam broadening effect during tropospheric observation. However, further analysis of improvements, including sidelobe suppression effects, is challenging owing to the nonuniform volume targets, necessitating the use of clear hard targets. In this study, beamwidth verification was performed using the moon compared with the calculated antenna pattern, which satisfies this condition. By utilizing the moon reflection echoes, we expect that various applications of the MIMO radar can be verified, and further combinations of multibeam and/or advanced beamforming techniques will be applied through this validation.

In general, few approaches exist to confirm the beamwidth directly. However, using the moon's reflection echo, which has been examined with the MU radar, could be one method to verify the beamwidth [10]. The observations with the moon reflection echoes and results are presented after discussions on the signal model of the MIMO radar and revised system of the MU radar. Furthermore, the combination of the MIMO virtual antenna and adaptive beamforming technique is expected to extract better performance, which was introduced in [11]. The Capon beamformer technique

was used with the MU radar for two-dimensional generalization of the brightness distribution in [12]; therefore, it is natural extension to confirm this combination effect.

This paper describes DDMA-MIMO observations using the MU radar by comparing it with other methods and discussing the signal model of the MIMO radar. The fundamental principle of the MIMO radar and adaptive beamforming methods are presented in Sect. 2. Four major methods to ensure the orthogonality of the transmit signals from the MIMO radar and the reasons for selecting the DDMA-MIMO for the MU radar are presented in Sect. 3. The system configuration of the MU radar as a MIMO radar and the observation results using the reflection echoes off the moon are presented in Sect. 4. Finally, the effectiveness of the MIMO radar is presented in Sect. 5.

2. Basic Theory

2.1 Basic Principle of the MIMO Radar

The MIMO technique has a long history. The wireless communications community has studied the characteristics and characterizations of the MIMO radar. In this section, the basic principle is introduced, as summarized in [1], [13]–[15].

Let there be M transmit signals. Let the m-th transmit signal be $x_m(t,\theta_0) = a_m(\theta_0)\phi_m(t)$, and let the n-th receive signal $y_n(t,\theta_0)$ be defined as

$$\begin{aligned} y_n(t,\theta_0) &= \alpha b_n(\theta_0)\sum_{m=1}^{M} a_m(\theta_0)\phi_m(t) + v_n(t) \\ &= \alpha b_n(\theta_0)\mathbf{a}(\theta_0)^{\mathrm{T}}\boldsymbol{\phi}(t) + v_n(t), \end{aligned} \tag{1}$$

where $v_n(t)$ represents the receive noise, $a_m(\theta_0)$ and $b_n(\theta_0)$ represent the transmit and receive phase shifts corresponding to the transmit target angle θ_0, $\boldsymbol{\phi}(t) \in \mathbb{C}^M$ is a normalized transmit waveform column vector composed of M transmitters, $\mathbf{a}(\theta_0) \in \mathbb{C}^M$ is a transmit steering column vector corresponding to the transmission angle θ_0, and α is a (complex-valued) backscatter coefficient.

To expand $y_n(t,\theta_0)$ to N receivers, the receive signal column vector $\mathbf{y}(t,\theta_0) \in \mathbb{C}^N$ is defined as

$$\mathbf{y}(t,\theta_0) = \alpha\mathbf{b}(\theta_0)\mathbf{a}(\theta_0)^{\mathrm{T}}\boldsymbol{\phi}(t) + \mathbf{v}(t), \tag{2}$$

where $\mathbf{b}(\theta_0) \in \mathbb{C}^N$ is the receive steering column vector that corresponds to the receive angle θ_0 (here, the transmit and receive angles are defined to be the same), and $\mathbf{v}(t) \in \mathbb{C}^N$ is the receive noise-column vector. Notably, $\mathbf{b}(\theta_0)\mathbf{a}(\theta_0)^{\mathrm{T}}$ represents an $N \times M$ matrix, that is, $\mathbf{b}(\theta_0)\mathbf{a}(\theta_0)^{\mathrm{T}} \in \mathbb{C}^{(N,M)}$.

Following range processing with time lag τ and matched filters $\boldsymbol{\phi}(t-\tau)^{\mathrm{H}}$ (the suffix H indicates a Hermitian transpose) to separate the transmit waveforms. The receive signal matrix $\mathbf{Z}(\tau,\theta_0) \in \mathbb{C}^{(N,M)}$ is expressed as

$$\begin{aligned} \mathbf{Z}(\tau,\theta_0) &\equiv \int_{-\infty}^{\infty} \mathbf{y}(t,\theta_0)\boldsymbol{\phi}(t-\tau)^{\mathrm{H}}\mathrm{d}t \\ &= \alpha\mathbf{b}(\theta_0)\mathbf{a}(\theta_0)^{\mathrm{T}}\int_{-\infty}^{\infty} \boldsymbol{\phi}(t)\boldsymbol{\phi}(t-\tau)^{\mathrm{H}}\mathrm{d}t \\ &\quad + \int_{-\infty}^{\infty} \mathbf{v}(t)\boldsymbol{\phi}(t-\tau)^{\mathrm{H}}\mathrm{d}t \\ &= \alpha\mathbf{b}(\theta_0)\mathbf{a}(\theta_0)^{\mathrm{T}}\mathbf{R}_{\phi}(\tau) + \mathbf{E}(\tau), \end{aligned} \tag{3}$$

where

$$\mathbf{R}_{\phi}(\tau) \equiv \int_{-\infty}^{\infty} \boldsymbol{\phi}(t)\boldsymbol{\phi}(t-\tau)^{\mathrm{H}}\mathrm{d}t \quad \in \mathbb{C}^{(M,M)} \tag{4}$$

represents the $M \times M$ MIMO signal correlation matrix that describes the correlation among the transmit waveforms, and

$$\mathbf{E}(\tau) \equiv \int_{-\infty}^{\infty} \mathbf{v}(t)\boldsymbol{\phi}(t-\tau)^{\mathrm{H}}\mathrm{d}t \quad \in \mathbb{C}^{(N,M)} \tag{5}$$

represents the filtered receive noise matrix.

The $N \times M$ data matrix expressed in (3) can be vectorized by stacking the columns of $\mathbf{Z}(\tau,\theta_0)$, and we define the receive MIMO signal as

$$\mathbf{z}(\tau,\theta_0) \equiv \mathrm{vec}[\mathbf{Z}(\tau,\theta_0)] \quad \in \mathbb{C}^{(NM,1)}. \tag{6}$$

Equation (6) is rewritten using the well-known relationships of the vectorization operator shown in [16]:

$$\begin{aligned} \mathrm{vec}\{\mathbf{XYZ}\} &= \{\mathbf{Z}^{\mathrm{T}} \otimes \mathbf{X}\}\mathrm{vec}\{\mathbf{Y}\}, \\ \mathrm{vec}\{\mathbf{XYZ}\} &= \{\mathbf{Z}^{\mathrm{T}} \otimes \mathbf{I}_N\}\mathrm{vec}\{\mathbf{XY}\}, \\ \mathrm{vec}\{\mathbf{XY}^{\mathrm{T}}\} &= \{\mathbf{Y} \otimes \mathbf{X}\}, \end{aligned} \tag{7}$$

where $\mathbf{X}$ represents an arbitrary $N \times K$ matrix, $\mathbf{Y}$ represents an arbitrary $K \times L$ matrix, $\mathbf{Z}$ represents an arbitrary $L \times N$ matrix, $\mathbf{I}_N$ represents a unit matrix of $N \times N$, and "$\otimes$" symbolizes the Kroneker product,

$$\begin{aligned} \mathbf{z}(\tau,\theta_0) &= \mathrm{vec}[\alpha\mathbf{b}(\theta_0)\mathbf{a}(\theta_0)^{\mathrm{T}}\mathbf{R}_{\phi}(\tau)] + \mathrm{vec}[\mathbf{E}(\tau)] \\ &= \alpha[\mathbf{R}_{\phi}^{\mathrm{T}}(\tau) \otimes \mathbf{I}_N]\mathrm{vec}[\mathbf{b}(\theta_0)\mathbf{a}(\theta_0)^{\mathrm{T}}] + \mathrm{vec}[\mathbf{E}(\tau)] \\ &= \alpha[\mathbf{R}_{\phi}^{\mathrm{T}}(\tau) \otimes \mathbf{I}_N][\mathbf{a}(\theta_0) \otimes \mathbf{b}(\theta_0)] + \mathrm{vec}[\mathbf{E}(\tau)] \\ &\equiv \alpha\mathbf{s}(\tau,\theta_0) + \mathbf{e}(\tau), \end{aligned} \tag{8}$$

where the MIMO steering vector $\mathbf{s}(\tau,\theta_0)$ for beam angle θ_0 and filtered noise columns vector $\mathbf{e}(\tau)$ are defined as

$$\mathbf{s}(\tau,\theta_0) \equiv [\mathbf{R}_{\phi}^{\mathrm{T}}(\tau) \otimes \mathbf{I}_N][\mathbf{a}(\theta_0) \otimes \mathbf{b}(\theta_0)] \tag{9}$$

$$\mathbf{e}(\tau) \equiv \mathrm{vec}[\mathbf{E}(\tau)]. \tag{10}$$

If it is assumed that the transmit signals $\boldsymbol{\phi}(t)$ are orthogonal with each other ($\phi_m(t)$ and $\phi_{m'}(t)$ $(m \neq m')$ are zero-correlation) and that each matched filtered range response is identical (each transmitter has the identical transmit waveform) and defined as $R_{\phi}(\tau)$, then each element of the MIMO signal correlation matrix can be expressed as

$$\begin{aligned} \mathbf{R}_{\phi}(\tau)_{m,m'} &\equiv \int_{-\infty}^{\infty} \phi_m(t)\phi_{m'}^{*}(t-\tau)\mathrm{d}t \\ &= \begin{cases} R_{\phi}(\tau), & (\text{for } m = m') \\ 0, & (\text{for } m \neq m') \end{cases} \end{aligned} \tag{11}$$

and (8) can be rewritten as

$$\mathbf{z}(\tau,\theta_0) = \alpha R_{\phi}(\tau)[\mathbf{a}(\theta_0) \otimes \mathbf{b}(\theta_0)] + \mathbf{e}(\tau). \tag{12}$$

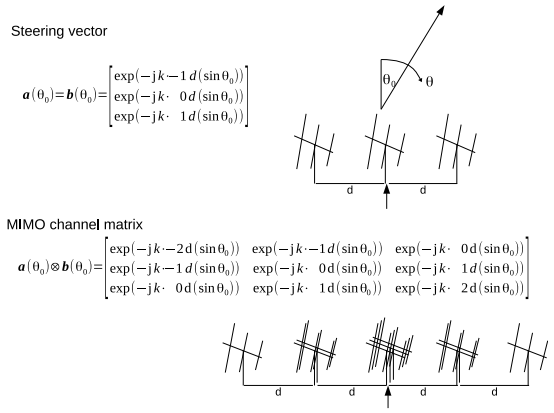

Fig. 1 Schematic of the MIMO radar for $M = 3$ transmitters and $N = 3$ receivers in one-dimension.

According to (12), the MIMO radar can be expanded to receive signal vectors using the MIMO channel matrix, which includes its transmit freedom, which can be expressed as $\mathbf{a}(\theta_0) \otimes \mathbf{b}(\theta_0) \in \mathbb{C}^{(NM,1)}$. Figure 1 shows a schematic of the MIMO radar with one-dimensional orthogonality of the transmit signals for $M = N = 3$.

2.2 SIMO and MIMO Adaptive Beamforming

The characteristics of the MIMO radar, which has a narrower receive and a wider transmit beam, are expected to work effectively for beamforming on a receiver referred to as the Capon beamformer, which generates angular brightness distribution. In this section, the Capon beamformer and its application to SIMO and MIMO radars are introduced.

In general, the output power $P_{BF}(\tau, \theta, \theta_0)$, obtained using the beamformer method at the range response time τ and the arrival angle θ, is expressed as [17], [18]

$$P_{BF}(\tau, \theta, \theta_0) = \frac{\mathbf{b}(\theta)^{\mathrm{H}} \mathbf{R}_z(\tau, \theta_0) \mathbf{b}(\theta)}{\mathbf{b}(\theta)^{\mathrm{H}} \mathbf{b}(\theta)} \tag{13}$$

and that obtained using the Capon beamformer, $P_{CP}(\tau, \theta, \theta_0)$, is [17]–[19]

$$P_{CP}(\tau, \theta, \theta_0) = \frac{1}{\mathbf{b}(\theta)^{\mathrm{H}} \mathbf{R}_z(\tau, \theta_0)^{-1} \mathbf{b}(\theta)}, \tag{14}$$

where $\mathbf{b}(\theta)$ represents the receive steering vector, and $\mathbf{R}_z(\tau, \theta_0)$ represents the covariance matrix of the receive signal vector $\mathbf{z}(\tau, \theta_0)$ [20], [21].

As shown earlier, MIMO radar processing is regarded as a virtual array of $M \times N$ elements. Therefore, the output power of the MIMO radar, obtained using the two methods, $P_{BF\text{–}MIMO}(\tau, \theta, \theta_0)$ and $P_{CP\text{–}MIMO}(\tau, \theta, \theta_0)$, are defined by replacing $\mathbf{b}(\theta)$ with $\mathbf{a}(\theta) \otimes \mathbf{b}(\theta)$ in (13) and (14), respectively [11],

$$P_{BF\text{–}MIMO}(\tau, \theta, \theta_0) = \frac{[\mathbf{a}(\theta) \otimes \mathbf{b}(\theta)]^{\mathrm{H}} \mathbf{R}_{z\text{–}MIMO}(\tau, \theta_0) [\mathbf{a}(\theta) \otimes \mathbf{b}(\theta)]}{[\mathbf{a}(\theta) \otimes \mathbf{b}(\theta)]^{\mathrm{H}} [\mathbf{a}(\theta) \otimes \mathbf{b}(\theta)]} \tag{15}$$

and

$$P_{CP\text{–}MIMO}(\tau, \theta, \theta_0) = \frac{1}{[\mathbf{a}(\theta) \otimes \mathbf{b}(\theta)]^{\mathrm{H}} \mathbf{R}_{z\text{–}MIMO}(\tau, \theta_0)^{-1} [\mathbf{a}(\theta) \otimes \mathbf{b}(\theta)]}, \tag{16}$$

where $\mathbf{R}_{z\text{–}MIMO}(\tau, \theta_0)$ represents the covariance matrix of the receive MIMO signal vector $\mathbf{z}(\tau, \theta_0)$ derived from (12) with the expression of a vector of expected values $E[\mathbf{x}]$ as

$$\mathbf{R}_{z\text{–}MIMO}(\tau, \theta_0) = E[\mathbf{z}(\tau, \theta_0) \mathbf{z}(\tau, \theta_0)^{\mathrm{H}}]. \tag{17}$$

3. Transmit Methods to Acquire Orthogonal Waveforms to be Determined for the MU Radar

Transmit/signal processing methods and system evaluation have attracted attention to ensure orthogonality of the transmit signal for the MIMO radar. In this section, four major methods introduced in [4] are discussed briefly, and the DDMA method is chosen for the MU radar.

3.1 Time Division Multiple Access (TDMA)

To guarantee transmit signal orthogonality by time separation, TDMA can be realized in a manner such that each transmit signal radiates at different times from different positions. The hardware and software systems used for this method are relatively simple, making the design of a radar system more easy. However, this method requires an adequate waiting time while other transmitters radiate; that is, it requires more dwell time. For the reasons mentioned earlier, the TDMA method requires a tolerance of the inter-pulse period times the number of MIMO transmitters (which also indicates duty ratio reduction), for the target identity, which is disadvantageous for atmospheric or weather radars. To overcome this effect, the staggered-TDMA method was introduced [4]. However, this method is restrictive, and it is only effective for low-frequency radars with continuous waves (CW).

3.2 Frequency Division Multiple Access (FDMA)

FDMA can be realized such that each transmit signal radiates at different frequencies in one time-series duration. The orthogonality of the transmitters guarantees that their signals can be extracted by a receiver using band-pass filters for each frequency, which would otherwise require certain frequency resources [22]. Therefore, the implementation cost of FDMA is relatively small. However, differences in the transmit frequencies can severely affect beamforming owing to the deterioration of the range sidelobes. To rectify this effect, FDMA using transmit frequencies that circulate toward slow-time is introduced, which also has certain limitations. To practically use atmospheric or weather radars, the influence of the range sidelobes should be reduced below an acceptable level.

Table 1 Comparison between orthogonal waveforms.

Method	Time division multiple access (TDMA)	Frequency division multiple access (FDMA)	Doppler division multiple access (DDMA)	Code division multiple access (CDMA)
Advantage	Good orthogonality	Good orthogonality	Good orthogonality	Approx. orthogonality Widely applicable
Judgment to be acceptable	Time loss Transmit power loss	High range sidelobe	Wide Doppler unambiguity	System costs, adequate correlation time
Add. approach for improvement	Staggered TDMA	Circulated FDMA	-	Slow-time CDMA CDMA with CCC

3.3 Doppler Division Multiple Access (DDMA)

DDMA can be realized using the principle of Doppler shift caused by the pulse-to-pulse phase difference. Each transmitter is set to its own initial phase per inter-pulse-period to generate a unique phase difference, which following transformation to the frequency division toward slow-time direction, divides the different frequency (Doppler) distribution. It has excellent transmit signal orthogonality, which makes it easier to configure the radar system.

DDMA can also achieve its objective using slightly different frequencies for the transmit waveforms to generate pulse-to-pulse phase differences [7], [23].

However, DDMA requires wide Doppler unambiguity to achieve transmit signal orthogonality. To satisfy this requirement, low transmit frequency and/or short inter-pulse period (short-range) radar systems are preferred. Therefore, a VHF radar such as the MU radar performs well, whereas a weather radar with a C-band or X-band must consider the trade-off between the observation range, maximum Nyquist velocity, and the number of orthogonal transmitters to apply this technique.

3.4 Code Division Multiple Access (CDMA)

CDMA can be realized such that orthogonal codes are used for the transmitters. The modulated transmit signals radiate to the target simultaneously and the returned signals are decoded by using the transmit codes for each signal. These codes are selected to be orthogonal to each other, such that the signals are completely separated by decoding their own codes in one receiver. This method has been widely employed, particularly in communication systems, for frequency efficiency, noise reduction, and high confidentiality.

Radar systems can apply CDMA to high range sidelobes but only in the fast-time direction. However, CDMA can easily overcome this disadvantage when slow-time direction is used. As one of the solutions, CDMA with complete complimentary codes (CCC) was proposed in [24] and [25], which has complementary codes to mitigate range sidelobes and eliminate all cross correlations in each code, such that their orthogonality to both fast-time and slow-time direction remains. Although CCC has development problems regarding the Doppler sidelobes for fast moving targets, atmospheric and weather radars can be applied owing to the relatively small the target velocity.

3.5 Optimal Method for the MU Radar

Four methods to realize the MIMO radar are introduced in previous subsections. Table 1 and Fig. 2 present comparisons between the orthogonal waveforms. Conventional SIMO radars are commonly used to identify a MIMO radar. The MU radar is one of the most multi-functional radars, which also functions as a MIMO radar with additional settings. From the previous discussion, DDMA and CDMA are suitable for the MU radar because it has lower frequencies and the Doppler speeds of the targets are relatively small. CDMA would be the best for higher frequency radars. However, it requires multiple transmitters with an independent pulse code setting. In contrast, DDMA can be modified to use multiple frequency sources to generate orthogonal waveforms. In this study, DDMA was chosen considering its easier application to the MU radar.

4. Beamwidth Verification Using the Moon's Reflection

4.1 MU Radar System Configuration

The MU radar [2], located in Shigaraki, Shiga, Japan, has been operational as an atmospheric radar since 1984. It consists of 475 elements, comprising 19-element antennas multiplied by 25 sub-array digital receivers, operating in the VHF band at 46.5 MHz. Upgraded to a digital modulator with frequency hopping functionality, it has 29 digital receivers for adaptive beamforming, including 25 primaries plus, an additional 4 receivers, as detailed in [20]. Although categorized as a SIMO radar, the MU radar can also function as a MIMO radar owing to its flexibility.

To use the MU radar as a DDMA-MIMO radar, we classified the transmit antennas into six parts, which is the same as the number of synchronized signal generators that have slightly different frequencies. In each receiver, the six orthogonal transmitter signals are separated using Doppler matched filters, which means that it consists of $6 \times 25 = 150$ receivers. Figure 3 shows images of the actual transmit and virtual receive antennas.

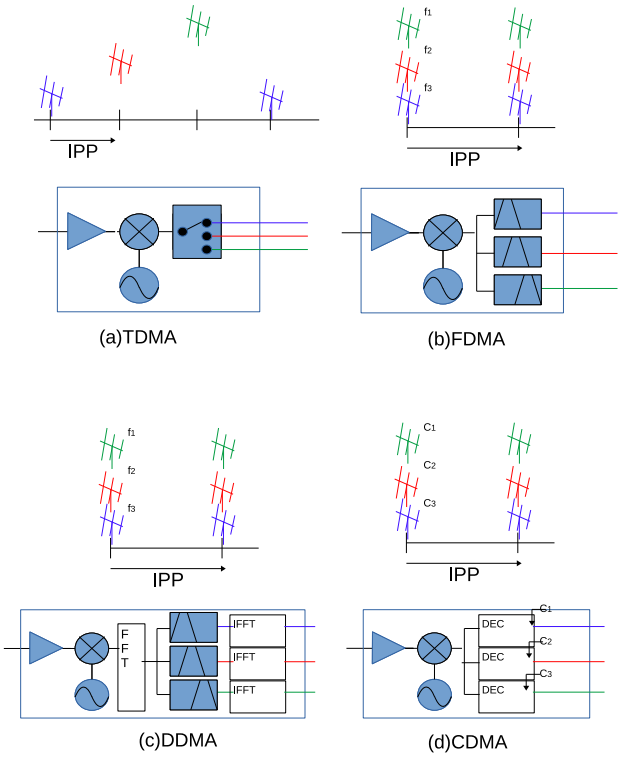

Fig. 2 Comparison between orthogonal waveforms (Configuration image).

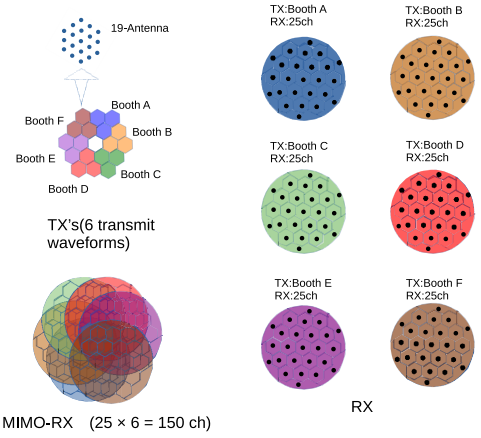

Fig. 3 Layout images of the actual transmit antenna (upper left), receive antenna (right), and virtual receive antenna (lower left).

4.1.1 Transmitter Configuration

The MU radar radiates a 46.5 MHz RF transmit signal by mixing a 5 MHz modulated IF-signal with a 41.5 MHz CW-local signal. In our study, the CW-local signal is used to replace the original signal with six separated local signals generated independently using signal generators but synchronized using a GPS-10 MHz oscillator. The frequencies of the signal generators are configured with intervals of f_{md} Hz between them to generate a pulse-to-pulse phase difference of $2\pi f_{md} T_{IPP}$ radians, where T_{IPP} is the inter-pulse period,

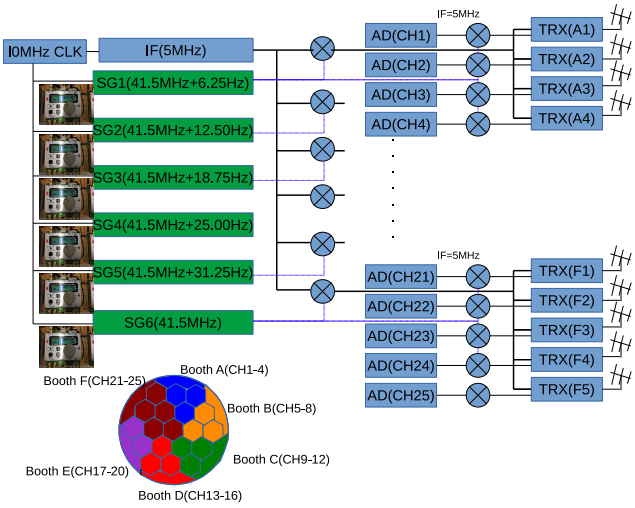

Fig. 4 DDMA-MIMO configuration of the MU radar. The green mark indicates additional settings, and the six orthogonal signals are distributed to the transmitters.

and each demodulator is processed by IF signals of 5 MHz, therefore down-converters by the same CW-local signals are equipped. The MIMO configuration of the MU radar is illustrated in Fig. 4.

4.1.2 Receiver Configuration

The receive signals that correspond to each transmit signal are mixed before the signal processing stage. A Doppler filter toward the slow-time direction is applied to separate the receive signals into orthogonal signals in the receiver.

Each receiver received six orthogonal waveforms, which were separated using Doppler filters. In this experiment, the interval of the Doppler offset velocity was selected to be $V_{Nyquist}/16 = 20.15\,\mathrm{ms}^{-1}$ because it is divisible by FFT points and enables us to consider the minimum frequency setting unit (0.01 Hz) of the SG, where $V_{Nyquist}$ is the Nyquist velocity, which is determined by the inter-pulse period, coherent integration number, and transmit frequency.

Because IF signals are down-converted by each transmit local signal, Doppler positions of the receive signal depend on the attributes of the receiver. Table 2 lists the Doppler offsets of the signal received from 25 receivers corresponding to the transmitters. In actual signal processing, amplitude and phase offset occurs because of the independent transmitters, which must be corrected on the receiver. The transmission phase adjustment process is presented in [9].

4.1.3 Antenna Position of the MU Radar

Figures 5 and 6 display the transmit and receive antenna positions of the MU radar, respectively. The transmit antennas are divided into six groups of sub-array antennas (composed of 57 antenna elements) that correspond to each antenna booth (depicted as booths A (A2/A3/A4 in blue); B (B2/B3/B4 in orange); C (C2/C3/C4 in green); D (D2/D3/D4

Table 2 DDMA-MIMO frequency settings (local signal frequency) and receive signal Doppler offset in each receiver.

Transmitter	Local signal frequency	Receive signal Doppler offset					
		A1-A4 CH1-CH4	B1-B4 CH5-CH8	C1-C4 CH9-CH12	D1-D4 CH13-CH16	E1-E4 CH17-CH20	F1-F5 CH21-CH25
TX1 (Booth A)	41.5 MHz + 6.25 Hz	0 ms^{-1}	20.15 ms^{-1}	40.29 ms^{-1}	60.44 ms^{-1}	80.59 ms^{-1}	-20.15 ms^{-1}
TX2 (Booth B)	41.5 MHz + 12.50 Hz	-20.15 ms^{-1}	0 ms^{-1}	20.15 ms^{-1}	40.29 ms^{-1}	60.44 ms^{-1}	-40.29 ms^{-1}
TX3 (Booth C)	41.5 MHz + 18.75 Hz	-40.29 ms^{-1}	-20.15 ms^{-1}	0 ms^{-1}	20.15 ms^{-1}	40.29 ms^{-1}	-60.44 ms^{-1}
TX4 (Booth D)	41.5 MHz + 25.00 Hz	-60.44 ms^{-1}	-40.29 ms^{-1}	-20.15 ms^{-1}	0 ms^{-1}	20.15 ms^{-1}	-80.29 ms^{-1}
TX5 (Booth E)	41.5 MHz + 31.25 Hz	-80.59 ms^{-1}	-60.44 ms^{-1}	-40.29 ms^{-1}	-20.15 ms^{-1}	0 ms^{-1}	-100.74 ms^{-1}
TX6 (Booth F)	41.5 MHz + 0 Hz	20.15 ms^{-1}	40.29 ms^{-1}	60.44 ms^{-1}	80.59 ms^{-1}	100.74 ms^{-1}	0 ms^{-1}

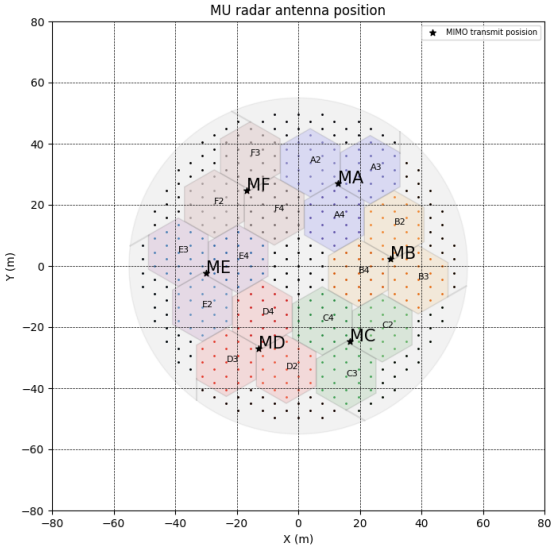

Fig. 5 Transmit antenna positions. Transmit antennas are divided into six groups of sub-array antennas (composed of 57 antenna elements) corresponding to the each booth (booth A (A2/A3/A4 in blue); B (B2/B3/B4 in orange); C (C2/C3/C4 in green); D (D2/D3/D4 in red); E (E2/E3/E4 in purple) and F (F2/F3/F4 in brown). Star markers denote the transmit antenna phase centers, and the black points are not used for transmission.

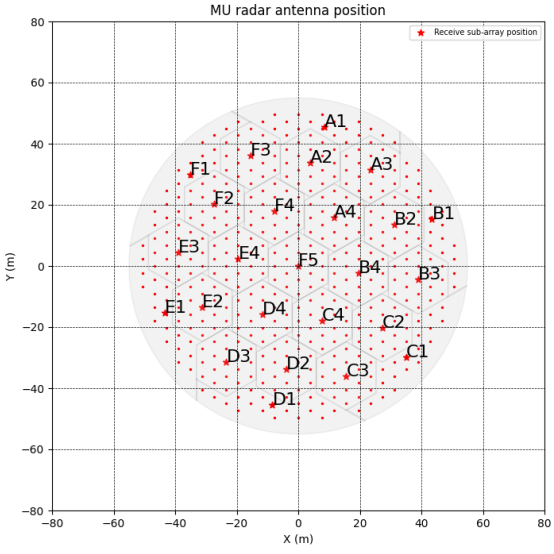

Fig. 6 Receive antenna positions. Star markers denote the receive antenna phase centers.

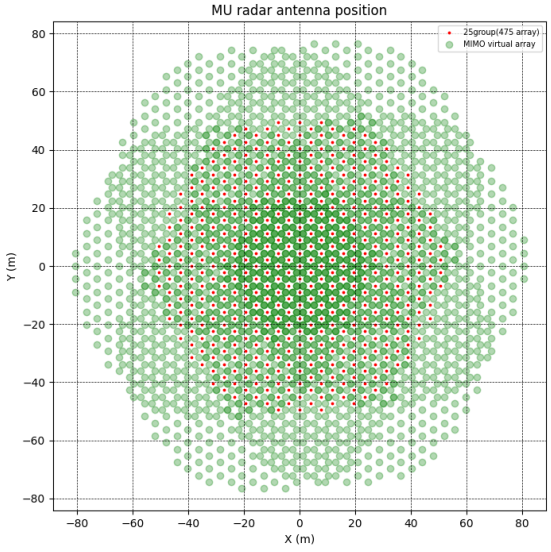

Fig. 7 Virtual receive antenna positions. The red points indicate the physical antenna layout, whereas the green dots represent virtual antennas. The green dots have transparency. The darker colors indicate overlapping antenna positions.

in red); E (E2/E3/E4 in purple); and F (F2/F3/F4 in brown). Star markers denote the transmit antenna phase centers, representing the transmit steering vector in Fig. 5, and highlight the receive steering vector in Fig. 6. These positions marked by stars correspond to the transmit steering vector $\mathbf{a}(\theta_0)$ and the receive steering vector $\mathbf{b}(\theta_0)$, representing the transmit and receive beam directions of θ_0, respectively.

4.1.4 Virtual Receive Antenna Position of the MU Radar for SIMO and MIMO

Figures 7 and 8 display the virtual receive and sub-array antenna positions for adaptive beamforming calculated using the MIMO channel matrix $\mathbf{a}(\theta_0) \otimes \mathbf{b}(\theta_0)$, respectively. The red points indicate the physical centers, and the green or blue dots indicate those of the virtual antennas. These dots have transparency, with darker colors indicating overlapping receiver positions. The receive MIMO antenna is larger than conventional physical ones, implying that MIMO-beamforming has narrower characteristics and sidelobe improvements compared with SIMO-beamforming.

4.2 Observation of the Moon's Reflection

As previously mentioned, MIMO radars can establish a virtual receive antenna aperture plane with transmission freedom. However, quantitatively confirming the enhancement of spatial resolution using observed atmospheric and ionospheric echoes is challenging owing to the nonuniform volume targets. To quantitatively assess the MIMO virtual array, we conducted observations of the beam pattern, as discussed by [10], derived from the reflection echo off the moon. We compared it with the calculated beam pattern from the virtual antenna layout.

4.2.1 Observation Parameters

The experiment was conducted for the 11th March, 2022 because the moon's position had a higher elevation angle (lower zenith angle), minimizing the radial velocity toward the radar, which made the analysis easier. The observation parameters are listed as experiment A presented in Table 3.

Figure 9 shows the time series of the estimated distance between the surface of the moon and observation point (Shigaraki, Japan), calculated using Skyfield (https://rhodesmill.org/skyfield/). From the estimation, the beam direction was determined for a zenith angle θ_0 of 8.59°, azimuth angle from the north ϕ_0 of 186.77° at 1849 JST 11th March, 2022, when the radial Doppler speed of the moon was expected to be zero when passing across the beam center.

For comparison, other experiments using conventional SIMO observations were conducted on the 27th June, 2022. The observation parameters and dates of these experiments are also listed in Table 3.

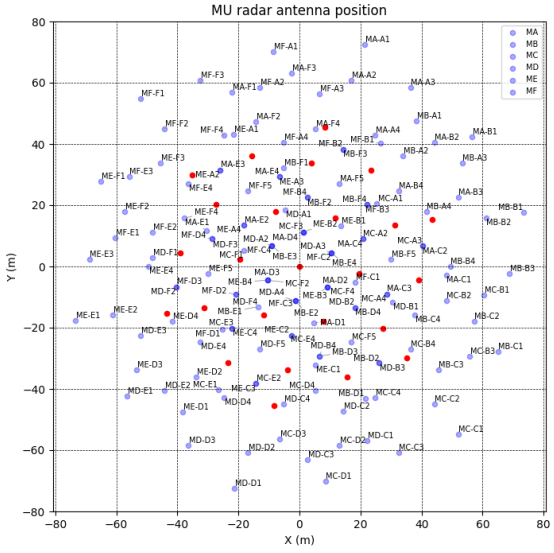

Fig. 8 Virtual receive sub-array positions for adaptive beamforming. The red points indicate the physical centers of the sub-array antennas, whereas the blue dots indicates those of the virtual sub-array antennas. The blue dots have transparency. The darker colors indicate overlapping antenna positions.

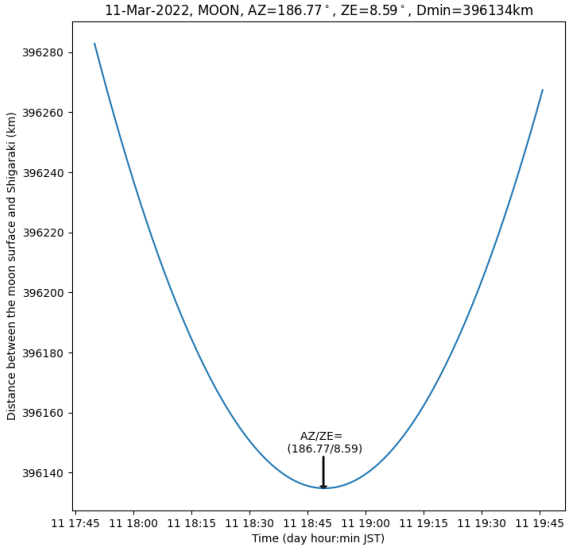

Fig. 9 Time series of estimated distance between the moon's surface and observation point (Shigaraki, Shiga, Japan) at 1750-1940 JST 11 Mar 2022 calculated using Skyfield (https://rhodesmill.org/skyfield/).

Table 3 Observation parameters and estimated distance from the MU radar to the moon's surface. Note this calculation does not consider the radius of curvature of the Earth or moon.

Item	Experiment A TX=57×6,RX=475×6(MIMO)	Experiment B TX=RX=475(SIMO)
Passing time of the beam center	1849 JST 11 Mar 2022	1008 JST 27 June 2022
Observation time	1750-1950 JST 11 Mar 2022	0920-1100 JST June 2022
Transmit antenna	57 (19 ×3ch) × 6	475 (19 × 25 ch)
Receive antenna	475 (19 ×25ch) × 6	475 (19 × 25 ch)
Inter-pulse period	10 000 μs	10 000 μs
Transmit beam direction (AZ/ZE)	186.77°/8.59°	166.24°/11.14°
Sub-pulse width	64 μs	64 μs
Pulse comp.	7bit Barker	7bit Barker
Coherent integration	1	1
FFT points	2 048	2 048
Estimated distance to the moon	396 134 km	396 903 km
N-th tripped echo	265	265
Estimated target range	412 km	1 180 km

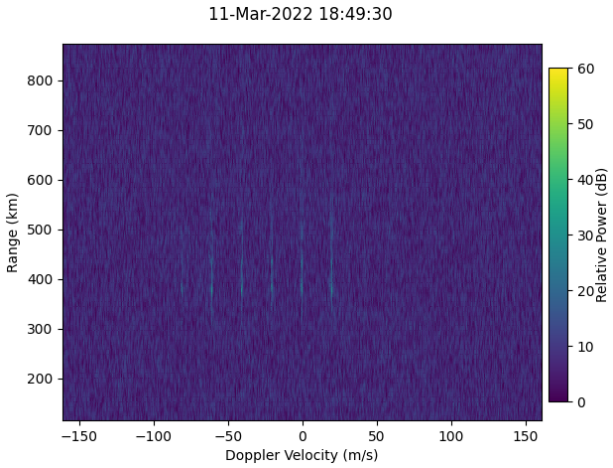

Fig. 10 Doppler spectra at A2 sub-array receivers observed at 1849 JST on 11 Mar 2022 before executing MIMO-processing. The horizontal and vertical axes show the target Doppler velocity and range with offset of 395 726 km due to echoes from 265 trips, respectively. Six receive signals derived from each orthogonal transmitter with DDMA-MIMO frequency offset (TX5, TX4, TX3, TX2, TX1, and TX6 from the left) were observed.

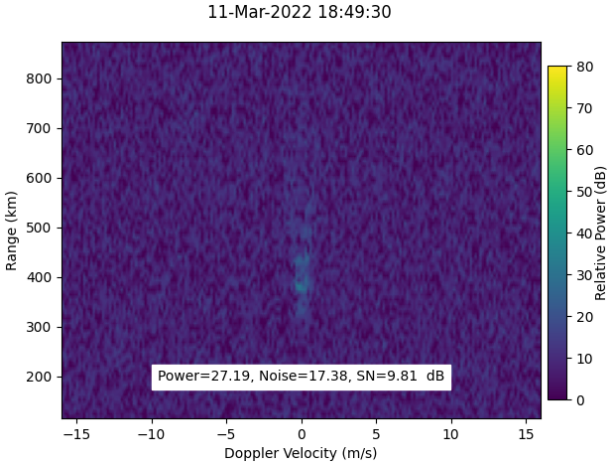

Fig. 11 Same as Fig. 10 except that the Doppler range was restricted from -16 to 16 ms^{-1}.

4.2.2 Observation Result: Doppler Spectrum of MIMO and SIMO Observation

Figure 10 illustrates the Doppler spectra obtained from the sub-array receivers A2 which is before executing MIMO-processing, where six separated signals received caused by transmit frequency offsets from the moon (265th trip echo) were confirmed.

In this figure, the estimated radial velocity of the moon was almost zero at the time of observation so that the observation results were consistent with those listed in Table 2, from which these signals could be identified as the signals received at TX5 ($-80.59\,\mathrm{ms}^{-1}$), TX4 ($-60.44\,\mathrm{ms}^{-1}$), TX3 ($-40.29\,\mathrm{ms}^{-1}$), TX2 ($-20.15\,\mathrm{ms}^{-1}$), TX1 ($0\,\mathrm{ms}^{-1}$), and TX6 ($20.15\,\mathrm{ms}^{-1}$)., respectively.

Figure 11 presents the same dataset as depicted in

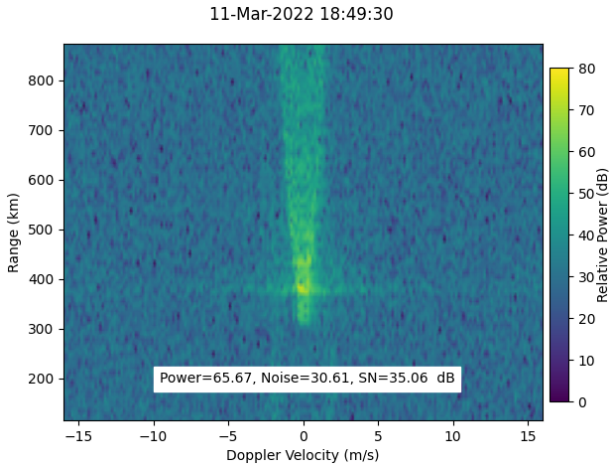

Fig. 12 Same as Fig. 11 except that the DDMA-MIMO processing was performed.

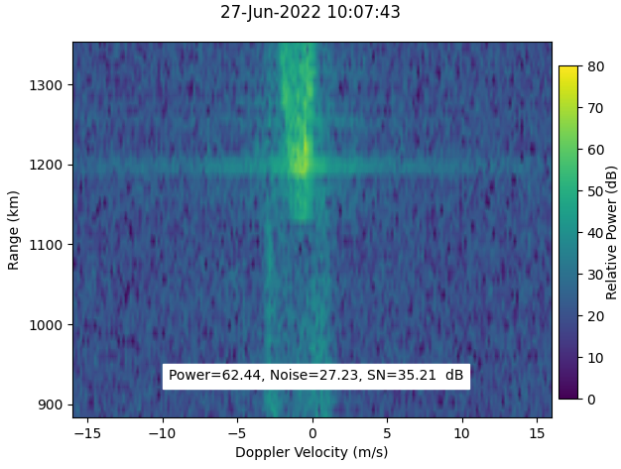

Fig. 13 Doppler spectra observed at 1007 JST on the 27th of June, 2022 as the conventional (SIMO) operation. The horizontal and vertical axes represent the target Doppler velocity and range with an offset of 395 726 km caused by echoes from 265 trips.

Fig. 10, with the Doppler range restricted from -16 to 16 ms^{-1}, where the signal-to-noise (S/N) ratio was calculated to be 9.81 dB. For a MIMO radar, the receive signals must be extracted using Doppler filters as independent IQ signals before combining them to obtain a MIMO receive signal by applying (12). Figure 12 illustrates the results after executing MIMO-processing, where the S/N ratio was calculated to be 35.06 dB. In this observation, the estimated summated power was the summation of 25×6 = 150 (21.76 dB) virtual receivers. Therefore, the summed S/N ratio was estimated to be 9.81+21.76=31.57 dB, where the difference in the observed data (Fig. 12) was considered to be caused by the individual difference (receive gain and the phase) in receivers.

Figure 13 shows the Doppler spectra observed at 1007 JST 27th June, 2022 as a conventional SIMO operation. This observation result was for a comparison between the MIMO and SIMO radars operated as experiment B, listed in Ta-

ble 3, where the S/N ratio was calculated to be 35.21 dB. From these results, the S/N ratio between the MIMO observation and the SIMO observation was also consistent from the point of the S/N ratio. Furthermore, the beam width appeared to be a wider distribution compared with that shown in Fig. 12. However, these differences are qualitative and cannot be definitively assessed.

4.2.3 Verification with the Beamformer and Capon

To verify the moon reflection echo quantitatively, we focus on the result whether the brightness distribution of the beamformer and the theoretical beam pattern comparing with the SIMO observation. Figures 14 and 15 show the two-dimensional angular imaging result of the moon's reflection echo. The MIMO observation data were the same as those used for the verification of the antenna pattern. As shown in Figs. 14 and 15, the MIMO radar had a narrower beamwidth than that of the SIMO radar.

Figure 16 illustrates the cut pattern at an azimuth angle of $\phi = 0^\circ$ to compare the MIMO and SIMO observation results with the receive antenna patterns. In this study, we compared the differences in power between the SIMO and MIMO beamformer and Capon methods. Specifically, the peak power was normalized for comparative analysis against the antenna pattern. The calculated peak differences between the beamformer and Capon brightness are indicated in Fig. 16, revealing differences of 2.65 dB for SIMO and 6.90 dB for MIMO. These differences are attributed to the influence of ionospheric scintillation on the observed data, which persists despite attempts to mitigate its effects through time-averaging. However, we confirmed that the Capon brightness with MIMO virtual arrays exhibited superior performance to that with SIMO physical arrays. Additionally, the dotted blue line (beamformer) and the red line (1-way antenna pattern) in the figure are consistent for both SIMO and MIMO observations, particularly in the mainlobe of both the SIMO and MIMO beamformer, indicating consistency

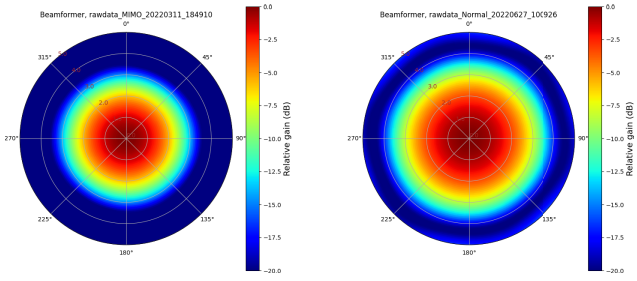

Fig. 14 Angular distribution of beamforming using the moon's reflection: Beamformer imaging result from MIMO (left) and SIMO (right) observations. Note that (azimuth, zenith) = (0,0) indicates the transmit beam direction.

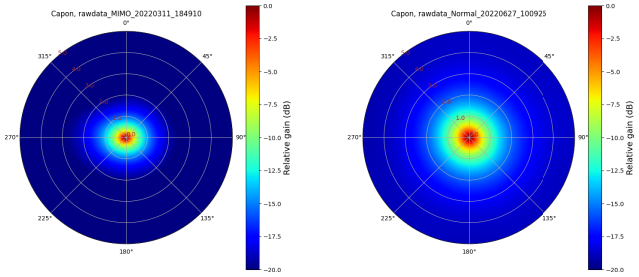

Fig. 15 Angular distribution of adaptive beamforming using the moon's reflection: Capon imaging result using MIMO (left) and SIMO (right) observations.

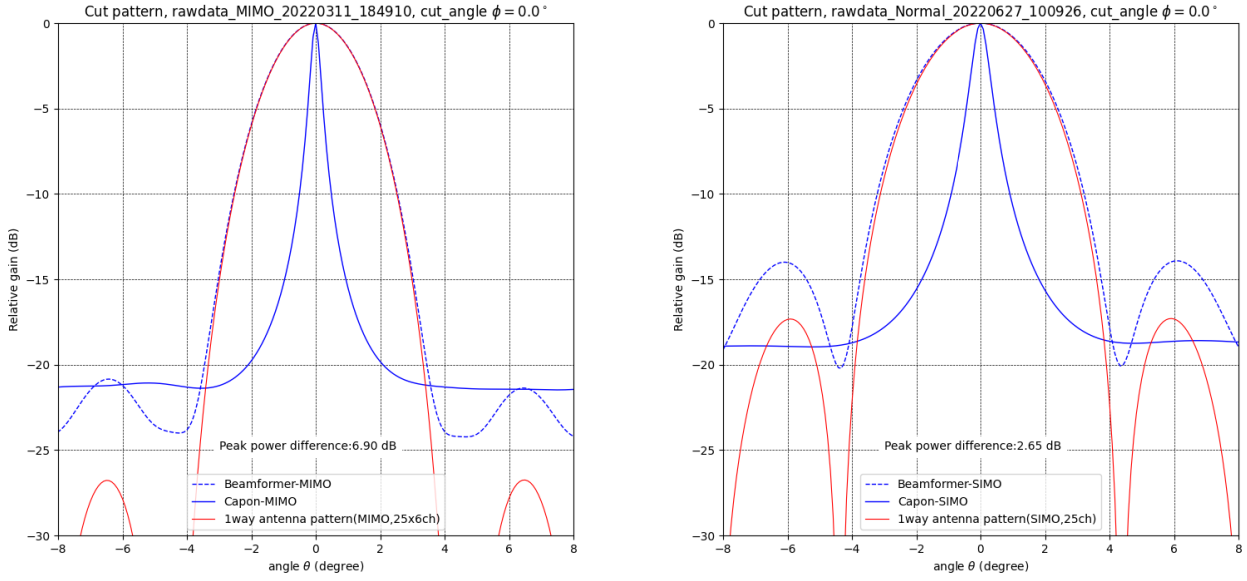

Fig. 16 Cut pattern at an azimuth angle of $\phi = 0^\circ$: Comparison between the beamformer, Capon, and calculated 1-way antenna pattern using MIMO (left) and SIMO (right) observations. The blue dotted and blue solid lines represent the angular distributions using the beamformer and Capon imaging, respectively, whereas the red line represents the calculated antenna pattern.

with theoretical expectations. Furthermore, Fig. 16 demonstrates the contribution of the virtual receive array to the suppression of antenna sidelobes, as predicted by theory.

The effectiveness of the Capon beamformer has already been demonstrated by [12], and the observation results were almost consistent. However, this experiment particularly showed that the Capon beamformer achieved even higher resolution when combined with MIMO radar, which the results clearly show.

From these results and considerations, the MU radar, in combination with the Capon beamformer, can operate as a MIMO radar with good performance and high angular resolutions.

5. Conclusion

In this study, an extension of the virtual receive array antenna that included the DDMA method was demonstrated through the experimental results using the MU radar, which was operated as a MIMO radar with additional settings. To achieve a DDMA-MIMO radar, local signals were replaced with six synchronized signal generators that generated different Doppler frequency offsets between the transmitters to realize transmit signal orthogonality. MIMO radar signal processing had a high compatibility with other processing methods, such as the Capon beamformer. It was confirmed through experimental results that a resolution finer than that of conventional methods can be obtained using a combination of the MIMO technique and Capon beamformer. Our findings are expected to contribute toward advancing the spatial super resolution technique intended for applications in atmospheric phased array radars.

Acknowledgments

The MU radar belongs to and is operated by the Research Institute for Sustainable Humanosphere (RISH), Kyoto University. This work was partially supported by ISHIZUE 2022 of Kyoto University and JSPS KAKENHI Grant Number JP23K17703.

References

[1] J. Li and P. Stoica, MIMO Radar Signal Processing, Wiley-IEEE Press, 2008.
[2] S. Fukao, T. Sato, T. Tsuda, S. Kato, K. Wakasugi, and T. Makihira, "The MU radar with an active phased array system: 1. Antenna and power amplifiers," Radio Sci., vol.20, no.6, pp.1155–1168, 1985.
[3] S. Kato, T. Tsuda, M. Yamamoto, T. Sato, and S. Fukao, "First results obtained with a middle and upper atmosphere (MU) radar," J. Atmos. Terr. Phys., vol.48, no.11-12, pp.1259–1267, 1986.
[4] H. Sun, F. Brigui, and M. Lesturgie, "Analysis and comparison of MIMO radar waveforms," 2014 Int. Radar Conf. Radar 2014, pp.1–6, 2014.
[5] J.M. Urco, J.L. Chau, M.A. Milla, J.P. Vierinen, and T. Weber, "Coherent MIMO to improve aperture synthesis radar imaging of field-aligned irregularities: First results at Jicamarca," IEEE Trans. Geosci. Remote Sens., vol.56, no.5, pp.2980–2990, 2018.
[6] J.M. Urco, J.L. Chau, T. Weber, and R. Latteck, "Enhancing the spatiotemporal features of polar mesosphere summer echoes using coherent MIMO and radar imaging at MAARSY," Atmos. Meas. Tech., vol.12, no.2, pp.955–969, 2019.
[7] D.J. Rabideau, "Doppler-offset waveforms for MIMO radar," IEEE Natl. Radar Conf. - Proc., pp.965–970, 2011.
[8] F. Yang, F. Xu, X. Yang, and Q. Liu, "DDMA MIMO radar system for low, slow, and small target detection," J. Eng., vol.2019, no.19, pp.5932–5935, 2019.
[9] T. Matsuda and H. Hashiguchi, "DDMA-MIMO observations with the MU radar: Validation by measuring a beam broadening effect," IEEE J. Sel. Topics Appl. Earth Observ., vol.16, pp.3083–3091, 2023.
[10] S. Fukao, T. Sato, T. Tsuda, M. Yamamoto, M.D. Yamanaka, and S. Kato, "MU radar: New capabilities and system calibrations," Radio Sci., vol.25, no.4, pp.477–485, 1990.
[11] H. Kimoto, N. Kikuma, and K. Sakakibara, "Target direction estimation characteristics of capon algorithm in MIMO radar," 2019 Int. Symp. Antennas Propagation, ISAP 2019 - Proc., 2019.
[12] R.D. Palmer, S. Gopalam, T.Y. Yu, and S. Fukao, "Coherent radar imaging using Capon's method," Radio Sci., vol.33, no.6, pp.1585–1598, 1998.
[13] M.S. Davis, Principles of Modern Radar: Advanced Techniques, Scitech publishing, 2013.
[14] M.S. Davis, G.A. Showman, and A.D. Lanterman, "Coherent MIMO radar: The phased array and orthogonal waveforms," IEEE Aerosp. Electron. Syst. Mag., vol.29, no.8, pp.76–91, 2014.
[15] M. Cattenoz, "MIMO radar processing methods for anticipating and compensating real world imperfections," Ph.D. dissertation, UniversitéParis Sud-Paris XI, Orsay, France, 2015.
[16] H.D. Macedo and J.N. Oliveira, "Typing linear algebra: A biproduct-oriented approach," Sci. Comput. Program., vol.78, no.11, pp.2160–2191, 2013.
[17] N. Kikuma, Adaptive Antenna Technology, Ohmsha, 2003 (in Japanese).
[18] H.L. Van Trees, Optimum Array Processing, Wiley-Interscience, New York, 2002.
[19] P. Stoica, Z. Wang, and J. Li, "Robust Capon beamforming," IEEE Signal Process. Lett., vol.10, no.6, pp.172–175, 2003.
[20] G. Hassenpflug, M. Yamamoto, H. Luce, and S. Fukao, "Description and demonstration of the new middle and upper atmosphere radar imaging system: 1-D, 2-D, and 3-D imaging of troposphere and stratosphere," Radio Sci., vol.43, no.2, 2008.
[21] J.S. Chen, C.Y. Wang, C.L. Su, and Y.H. Chu, "Meteor observations using radar imaging techniques and norm-constrained Capon method," Planet. Space Sci., vol.184, no.2020, p.104884, 2020.
[22] D. Cohen, D. Cohen, and Y.C. Eldar, "High resolution FDMA MIMO radar," IEEE Trans. Aerosp. Electron. Syst., vol.56, no.4, pp.2806–2822, 2020.
[23] D.J. Rabideau, "MIMO radar waveforms and cancellation ratio," IEEE Trans. Aerosp. Electron. Syst., vol.48, no.2, pp.1167–1178, 2012.
[24] J. Tang, N. Zhang, Z. Ma, and B. Tang, "Construction of Doppler resilient complete complementary code in MIMO radar," IEEE Trans. Signal Process., vol.62, no.18, pp.4704–4712, 2014.
[25] T. Kishigami, H. Yomo, N. Yosoku, A. Matsuoka, and J. Sato, "MIMO radar waveforms using orthogonal complementary codes with Doppler-offset," IEICE Trans. Commun., vol.E101-B, no.6, pp.1503–1512, June 2018.

Tomoya Matsuda received the B.S. and M.S. degrees in Department of electronic and communication engineering from Kyoto University, Japan, in 1997 and 1999, respectively. In 1999, he joined Mitsubishi Electric Corporation, Japan, where he has been engaged in development of active phased array radar system. His research interests include the development of phased array radar systems for atmospheric and weather radars. He was a recipient of the 2022 Gambo-Tatehira Award of the Meteorological Society of Japan on behalf of Mitsubishi Electric Corporation.

Koji Nishimura received his B.E. degree from Ritsumeikan University, Japan, in 1999, and his M.I. and Ph.D. degrees from Kyoto University, Japan, in 2001 and 2006, respectively. From 2001–2003, he worked for Sony Corporation. Since 2007, he was with the National Institute of Polar Research (NIPR), and the Research Organization for Information and Systems (ROIS), Tokyo, Japan. From 2021 to present, he has been with Kyoto University as an Associate Professor. His major research interests are radar signal processing, multi-channel and space-time signal processing, remote sensing for the atmosphere, and satellite communications. Dr. Nishimura was a recipient of the Commendation for Contributors to Promotion of an Oceanic State from the Prime Minister of Japan in 2015. He was a recipient of the Prize for Science and Technology from the Minister of Education, Culture, Sports, Science and Technology of Japan in 2014.

Hiroyuki Hashiguchi received Bachelor of Engineering from the Faculty of Engineering and Design, Kyoto Institute of Technology, Kyoto, Japan, in 1990. He completed the second half of his Ph.D. degree with the Department of Electrical Science and Engineering, Graduate School of Engineering, Kyoto University, Kyoto, in 1995. In 1997, he became a Research Associate with the Radio Atmospheric Science Center, Kyoto University (reorganized in 2000 as the Radio Science Center for Space and Atmosphere). In 2001, he became an Associate Professor at the Radio Science Center for Space and Atmosphere, Kyoto University [reorganized in 2004 as the Research Institute for Sustainable Humanosphere (RISH)]. In 2018, he became a Professor at RISH. His research interests include the development of atmospheric radars and research on observations using their radars. Dr. Hashiguchi is a member of the Meteorological Society of Japan, the Society of Geomagnetism and Earth, Planetary and Space Sciences, the American Meteorological Society, the American Geophysical Union, and the Institute of Electronics, Information and Communication Engineers, Japan. In 1992, he became Research Fellow of the Japan Society for the Promotion of Science. He was a recipient of the 2006 Minister of Education Science and Technology Award, and the 2008 Horiuchi Award and 2022 Gambo-Tatehira Award of the Meteorological Society of Japan.